Review article

Nusrat Jahan[a], Hanwei Wang[a], Shensheng Zhao, Arkajit Dutta, Hsuan-Kai Huang, Yang Zhao* and Yun-Sheng Chen*

Optical force microscopy: combining light with atomic force microscopy for nanomaterial identification

Abstract: Scanning probe techniques have evolved significantly in recent years to detect surface morphology of materials down to subnanometer resolution, but without revealing spectroscopic information. In this review, we discuss recent advances in scanning probe techniques that capitalize on light-induced forces for studying nanomaterials down to molecular specificities with nanometer spatial resolution.

Keywords: atomic force microscopy (AFM); chirality; nanostructures; optical forces; polarization; structured light.

1 Introduction

The foundation of today's scanning probe technique evolves from scanning tunneling microscope (STM) and atomic force microscope (AFM) pioneered by Binnig et al. [1, 2], where a sharp tip scans across a surface; the detection of surface morphology relies on tunneling current in STM [1] and van der Waals forces between atoms on the sample and atoms on the tip in AFM [2]. The limitation of traditional scanning probe microscopy is its blindness to materials. To bring the capability of identifying materials, recent research introduces light to the scanning probe techniques. In this review, we focus on two main approaches: one through material absorption of light and the other through dipole forces, both detectable through variations of nanoscale forces. Another technique that relies on light scattering by the nanomaterials facilitated by the scanning probe technique is the near-field scanning optical microscopy (NSOM) or scanning near-field optical microscopy (SNOM). Because of the quite different theoretical foundation and the detection mechanism, NSOM or SNOM is not within the scope of this review. References [3–10] represent a few recent reviews and key publications in NSOM/SNOM, which interested readers can follow through. Here we will focus on understanding particularly how light-induced forces through the above-mentioned two mechanisms can be applied to identify material properties. We will review the theoretical foundations and discuss the recent advances in experimental realizations on this topic. Rich material information such as chirality, optical, and chemical properties was investigated and revealed with nanoscale light-induced forces. These forces were too weak to be measurable in the past. Combining light-induced forces with atomic force microscope (AFM) provides a promising route towards studying nanomaterials down to molecular specificities.

2 Fundamental theory of optical forces

The light-matter interaction that gives rise to optically induced forces was at the heart of major breakthroughs in nanoscale imaging and manipulation of nanoscale to microscale objects. These optical forces which are associated with local electromagnetic field gradient, radiation

[a]**Nusrat Jahan and Hanwei Wang:** These authors contributed equally.
*Corresponding authors: Yang Zhao,** Department of Electrical and Computer Engineering, University of Illinois Urbana Champaign, Urbana, IL 61801, USA; and Holonyak Micro and Nanotechnology Laboratory, University of Illinois Urbana Champaign, Urbana, IL 61801, USA, e-mail: yzhaoui@illinois.edu. https://orcid.org/0000-0002-0154-3483; and **Yun-Sheng Chen,** Department of Electrical and Computer Engineering, University of Illinois Urbana Champaign, Urbana, IL 61801, USA; and Beckman Institute for Advanced Science and Engineering, University of Illinois Urbana Champaign, Urbana, IL 61801, USA, e-mail: yunsheng@illinois.edu. https://orcid.org/0000-0001-8823-970X
Nusrat Jahan, Hanwei Wang, Shensheng Zhao, Arkajit Dutta and Hsuan-Kai Huang: Department of Electrical and Computer Engineering, University of Illinois Urbana Champaign, Urbana, IL 61801, USA

pressure, and/or thermal expansion of materials, are of fundamental importance in applications ranging from optical trapping [11–20] to modern microscopy techniques [21–26].

2.1 Maxwell's stress tensor

The basic theory of optical forces can be derived from conservation law, where the time variation of the mechanical momentum of the matter ($\mathbf{P}_{mech}$) and the electromagnetic momentum ($\mathbf{P}_{em}$) can be described using Maxwell's stress tensor $\mathbf{T}$ enclosed in a surface S

$$\frac{d}{dt}(\mathbf{P}_{mech} + \mathbf{P}_{em}) = \int_S \mathbf{T} \cdot \mathbf{n} \, ds, \qquad (1)$$

where $\mathbf{n}$ is the normal vector of the surface, and S is an arbitrary closed surface that contains the particle. The first term on the left-hand side (rate of change of the mechanical momentum) denotes the force exerted on the particle by the electromagnetic field. The second term of the left-hand side denotes the rate of change of the electromagnetic momentum of the field within volume V

$$\frac{d}{dt}\mathbf{P}_{em} = \frac{1}{c^2}\frac{d}{dt}\int_V \mathbf{E} \times \mathbf{H} dV.$$

The components of the Maxwell's stress tensor are

$$T_{ij} = \varepsilon E_i E_j + \mu H_i H_j - \frac{1}{2}\delta_{ij}(\varepsilon E^2 + \mu H^2), \ i, j = 1, 2, 3 \qquad (2)$$

where ε (or μ) denotes the permittivity (or permeability) of the medium and E (or H) denotes the total electric (or magnetic) fields [27, 28]. Because of the $\frac{1}{c^2}$ factor, the $\frac{d}{dt}\mathbf{P}_{em}$ term is often much smaller in magnitude compared to the $\frac{d}{dt}\mathbf{P}_{mech}$ term.

Optical frequency is in the PHz to THz regime; because of this fast oscillation, time-averaged forces are often measured. If the electromagnetic field is time-harmonic, due to $\left\langle\frac{d}{dt}\mathbf{P}_{em}\right\rangle = 0$, the averaged observable force from the electromagnetic field is [29]

$$\langle\mathbf{F}\rangle = \left\langle\frac{d}{dt}\mathbf{P}_{mech}\right\rangle = \int_S \langle\mathbf{T}\rangle \cdot \mathbf{n} \, ds, \qquad (3)$$

where $\langle\rangle$ denotes time average. The time-averaged Maxwell's stress tensor elements are

$$\langle T_{ij}\rangle = \frac{1}{2}\text{Re}\left[\varepsilon E_i E_j^* + \mu H_i H_j^* - \frac{1}{2}\delta_{ij}(\varepsilon |E|^2 + \mu |H|^2)\right], \qquad (4)$$
$$i, j = 1, 2, 3$$

2.2 Dipole approximation

When a monochromatic light interacts with an object with scale much smaller than the wavelength, the object is often approximated into a spherical particle with radius a ($a \ll \lambda$). In the dipole approximation, the optical force experienced by subwavelength particles can be expressed as

$$\mathbf{F} = (\mathbf{p} \cdot \nabla)\mathbf{E} + \frac{1}{c}\dot{\mathbf{p}} \times \mathbf{B}, \qquad (5)$$

where $\mathbf{p}$ is the dipole moment of the particle induced by the electric field $\mathbf{E}$. The first part of the equation denotes the gradient force, which is often displayed as $\mathbf{F} = \frac{1}{2}\alpha_0 \nabla E^2$ in the Rayleigh regime [12, 30], and the second part denotes the scattering and absorbing forces that can be further displayed using scattering and absorption cross-section of the particle [12, 31].

The time averaged *total* force exerted on a small dielectric particle can be expressed as [31, 32]

$$\langle F_i\rangle = \frac{1}{2}\text{Re}\{\alpha E_j \partial^i E_j^*\}, \qquad (6)$$

where $i = x, y, z$ in the Cartesian coordinate, α is the polarizability of the small particle, including the radiation-reaction term, is described as $\alpha = \dfrac{\alpha_0}{1 - \frac{2}{3}ik^3\alpha_0}$. α_0 is the particle polarizability that satisfies the Clausius-Mossotti equation $\alpha_0 = 4\pi\varepsilon_0\varepsilon_m\left(\dfrac{\varepsilon_p - \varepsilon_m}{\varepsilon_p + 2\varepsilon_m}\right)a^3$, where a is the radius of the particle and ε_p is the relative permittivity of the particle and ε_m is the relative permittivity of the medium. To obtain Eq. (6), several assumptions need to be added: the particle is only polarizable by the electric field that excludes its magnetic response or bi-anisotropy, which means that $\mathbf{p} = \alpha\mathbf{E}$. In addition, the field is assumed to be monochromatic, where $\mathbf{B} = c/i\omega\nabla \times \mathbf{E}$.

To involve more generalized particles, Refs. [33–46] investigated conditions where not only electric but also magnetic and electromagnetic polarizabilities of the particles are considered. The general form of optical force is

$$\mathbf{F} = \mathbf{F}_e + \mathbf{F}_m + \mathbf{F}_{em}. \qquad (7)$$

The $\mathbf{F}_{em}$ term can give rise to detection of structural information of small particles using scanning probe technique that combines with optical forces.

Note that the second term in Eq. (5) contains optical forces originating from absorption, while in experiments the absorption-induced thermal expansion force is also detected. Note that this term is not included above. We will discuss it in the next section.

2.3 Thermal forces

Aside from optical gradient forces and radiation pressures, light-induced thermal forces (or photo-thermal forces) can be used in nanoscale spectroscopy [26, 47]. For example, near material absorption resonances, a temperature increment of the sample can give rise to thermal expansion. When detecting this photo-thermal expansion using AFM, a thermal expansion force is measured, which is also mediated by intermolecular interaction between the AFM tip and sample

$$F \approx \frac{\partial F_{ts}}{\partial z} \Delta L_{tot}(z), \tag{8}$$

where ΔL_{tot} is the total thermal expansion of the sample and F_{ts} is the intermolecular force between the tip and the sample. This intermolecular force consists of an attractive force in the noncontact region and a repulsive force in the contact region. The maximum photo-thermal expansion ΔL_{max} is described as [47]

$$\Delta L_{max} \approx \sigma d \Delta T_{max}, \tag{9}$$

where σ is the linear thermal expansion coefficient, d is the thickness of the sample, and $\Delta T_{max} \approx \frac{P_{abs}}{\rho C V_{heat}}$. Here, P_{abs} is the absorbed power, ρ is the density, C is the heat capacity, and V_{heat} is the heated volume related to the thermal diffusion length.

The generation of photo-thermal forces can be described as a series of processes: the absorbed power (P_{abs}) leads to a temperature rise (ΔT) in the sample, which results from the energy exchange between the tip and the sample; this temperature rise is in conjunction with the field enhancement mediated by the tip. The accumulated heat near the tip diffuses to the sample and deforms it, which in turn modulates the tip-sample distance (ΔL) and ultimately modulates the intermolecular force (ΔF). This total process can be expressed as [24]

$$\Delta F \sim \Delta L \sim \Delta T \sim P_{abs}, \tag{10}$$

3 Experimental realization of scanning probe techniques utilizing optical forces

In this section, we will discuss how to detect material properties using optical-induced forces, combined with AFM. AFM, as an effective method for weak force measurement with a nanometer-scale spatial resolution, provides a powerful tool for measuring optical-induced forces and using these optical forces to detect material properties. Many mechanisms have been involved in developing this new type of scanning probe technique for material identifications. As we introduced in the theoretical section, optical-induced forces can arise from gradient optical forces, scattering forces (radiation pressure), and/or absorption-induced forces [48]. A series of optical force-based microscopy techniques have recently been developed, including photo-induced force microscopy (PiFM – that mainly detects gradient force and radiation pressure), chiral optical force microscopy (COFM – that detects the gradient forces in conjunction with electromagnetic polarizabilities of the sample), photo-expansion microscopy or photo-thermal induced resonance (PTIR and AFM-IR – that detect absorption-induced forces), etc. Their principles, detection mechanisms, and applications are introduced in the following.

3.1 Principles of detection mechanisms

3.1.1 PiFM

When gradient force and radiation pressure dominate, as shown in Figure 1A, optical forces acting on an AFM tip consist of two parts: an attractive force given by the photo-induced dipole and a repulsive force given by radiation pressure [26, 48, 49, 51],

$$\langle F \rangle \propto F_{loc} + F_{nloc}. \tag{11}$$

References [24, 49, 51, 52] discussed the origin of these forces when detecting using AFM. The attractive force (denoted as F_{loc}) is caused by the attraction of induced dipole and its mirror images [49, 52] as shown in Figure 1B. This is true when a metallic AFM tip is used. When the tip-sample separation is much larger than the sample's as well as the tip's radii, the localized force can be approximated by Eq. (12), where the sample and the tip are assumed to be electric polarizable particles with polarizabilities α_s and α_t,
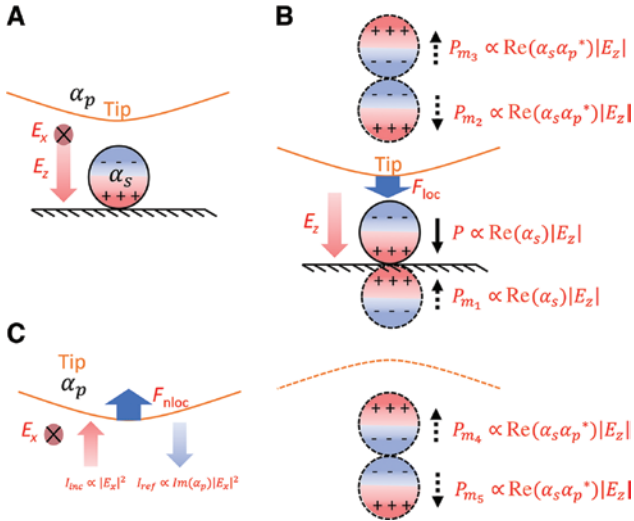
Figure 1: Optical forces detected by an atomic force microscope (AFM) tip [49, 50].
(A) Particle, tip, and electrical field; (B) photo-induced dipole (circled by black curve), and its mirror images (circled by black dashed curve). The dipoles create an attractive force to the tip, which decreases in z^{-4} with the distance between the tip and the particle. (C) Radiation pressure results in a nonlocalized force, which is independent of the tip position.

$$F_{loc} \propto -\frac{1}{z^4} \mathrm{Re}(\alpha_s \alpha_t^*)|E_z|^2, \tag{12}$$

where * denotes complex conjugate; z denotes the separation between the sample and the tip in the vertical direction; and E_z is the z component of the incident field. The F_{loc} is proportional to z^{-4}, which decays drastically as the tip-sample separation increases, therefore, this force is often referred to as local forces.

The nonlocalized force is induced by radiation pressure as shown in Figure 1C, which is given as

$$F_{nloc} \propto \mathrm{Im}(\alpha_t)|E_x|^2. \tag{13}$$

Here we mainly attribute the forces in PiFM to optical forces (gradient and radiation pressures). It is worth noting that Ref. [47] suggests that van der Waals force-mediated thermal expansion can also be accompanied in PiFM. Van der Waals force is distance-dependent, and its relation is given by

$$F_{ts}(z) \approx -\frac{H_{eff}R}{12}\frac{1}{H^2} \; (H \geq r_0), \tag{14}$$

where r_0, R, H, H_{eff} are the interatomic distance (~0.3 nm) that depends on the materials, radius of curvature of the tip, gap distance, and effective Hamaker constants. Thermal expansion decreases the gap distance between the sample and the tip, and therefore increases the van der Waals force acting on the tip.

3.1.2 PTIR and AFM-IR

The photo-thermal heating of sample surface causes a very small expansion ~10^{-3} Å. The average thermal expansion $\langle h_0 \rangle$ is given by [53]

$$\langle h_0 \rangle \propto \frac{\beta\alpha(\lambda)lP}{f\rho CA}, \tag{15}$$

where β is the linear thermal expansion coefficient of the solid, $\alpha(\lambda)l$ is the fraction of light absorbed as a function of the wavelength λ, P is the power of the laser beam, f is the modulation frequency of incident light, ρ is the density, C is the specific heat of the solid, and A is the area of laser beam.

The PTIR technique exploits this thermal expansion for chemical identification and imaging with a nanometer-scale resolution [22]. In PTIR, infrared (IR) laser pulses are absorbed by the sample, causing the sample's rapid expansion. As a result, the AFM cantilever deflects. The amplitude of the deflection, which is proportional to the absorbed energy, is measured in Ref. [54].

When the AFM cantilever is in contact with the sample surface, the cantilever deflection measures the thermal expansion [23, 55, 56]. Particularly, in Ref. [23], a free-electron laser with a pulse duration of ~10 µS is used as the IR source. As shown in Figure 2A, the tip is in contact with a single bacterium sample with a force of 10 nN; the illumination wavelength is chosen to align with the absorption peak of Amide I (the band is due to C=O stretching of the peptide bonds on the bacterium membrane); then a photo-thermal induced oscillation is detected from the AFM deflection signal. In Ref. [55], a quantum cascade laser (QCL) is used as the light source to generate laser pulses and the laser repetition rate is chosen to match the mechanical resonance frequency of the cantilever; the gold-coated AFM tip and the gold substrate dramatically enhances the optical field intensity between the tip and substrate. As a result, thermal expansion of an ultrathin sample layer ~2 nm is detected. Such a thin molecular layer corresponds to as few as 30 molecules. The typical spatial resolution using contact mode is 50 ~ 100 nm. The spatial resolution is limited by the properties of samples. For example, sample roughness can affect the spatial resolution.

To improve the spatial resolution up to ~10 nm, peak force IR microscopy (PFIR) was developed as Ref. [56]. PFIR measures the photo-thermal expansion of samples upon IR laser illumination by performing a map of force-distance curves, providing chemical and mechanical information simultaneously. When the tip approaches the sample surface, the pulsed IR laser illuminates the sample
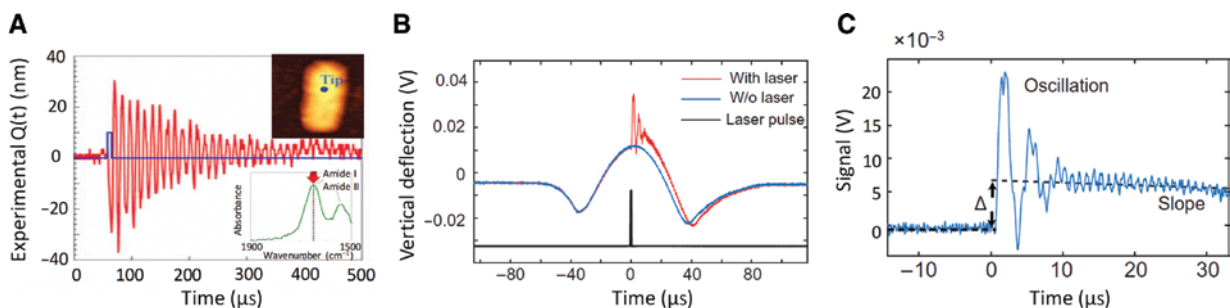
Figure 2: Detected signal of thermal expansion [23, 56].
(A) Deflection signal in contact mode; inset shows the topography of the bacterium sample; the position of AFM-tip is marked in blue dot; fourier transform infrared spectroscopy (FTIR) spectra in the right bottom inset; optical frequency is indicated by red arrow. (B) Signal by tapping mode; averaged traces of vertical deflections of the cantilever with and without laser interaction (red and blue curve). (C) Difference between the two curves in (B) (Figures adapted from Refs. [23, 56]).

to generate thermal expansion. The sample is in contact with the tip when the thermal expansion is measured via the deflection of the cantilever; while during the scanning of the sample surface, the tip lifts away from position to position, thus improving spatial resolution as well as releasing constraints, especially on sticky samples. As shown in Figure 2, an oscillation is detected by taking the difference of the vertical deflection of the cantilever with and without pulsed laser illumination (Figure 2B,C) [56]. The oscillation amplitude of the cantilever reflects the thermal expansion of the sample (instant and average expansion) that is proportional to the absorption coefficient, i.e. $\alpha(\lambda)$ in Eq. (15). This information can be used to identify the molecular spectrum on the sample surface.

While both PiFM and photo-thermal IR microscopy are based on forces originated from light, it remains challenging to differentiate their fundamental mechanisms. Yang and Raschke [48] suggested looking into the lineshapes of the measured forces, because noncontact optical forces and contact thermal forces are dominated by the real and imaginary part of the polarizability, respectively,

suggesting an asymmetric lineshape for the optical forces whereas symmetric lineshape for the thermal forces. In two separate studies [57, 58], noncontact piconewton range optical forces are directly measured with nonoscillating cantilevers.

3.1.3 Enhancing the signal-to-noise ratio using mechanical resonances

The optical-induced forces are often measured using the change of amplitude of the AFM cantilever (cantilever deflection signals). Therefore, the mechanical resonances of the cantilever are often used to improve the signal-to-noise ratio [59]. Figure 3A shows the AFM-IR spectrum measured using contact mode by varying the repetition rate of the laser to match the various mechanical frequencies of the cantilever; the measured signal shows two resonance peaks. When the laser repetition rate matches one of the mechanical resonance frequencies of the cantilever (Figure 3B), distinct photo-expansion signals are observed.
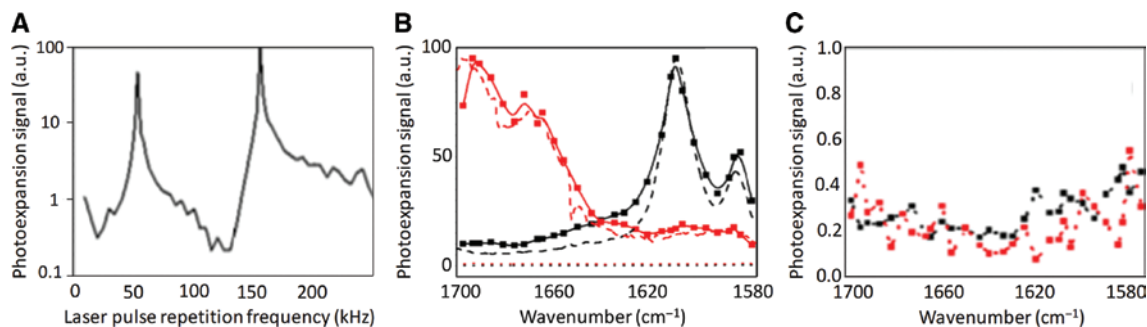
Figure 3: Enhancement of signal by matching the laser repetition rate with the cantilever's mechanical frequencies [59].
(A) Measured AFM signal using contact mode as a function of various laser pulse repetition rate. (B) AFM-infrared, IR spectrum with laser pulse repetition rate of 155 KHz (on resonance). (C) AFM-IR spectrum with laser pulse repetition rate of 130 KHz (off resonance) (Figures adapted from Ref. [59]).
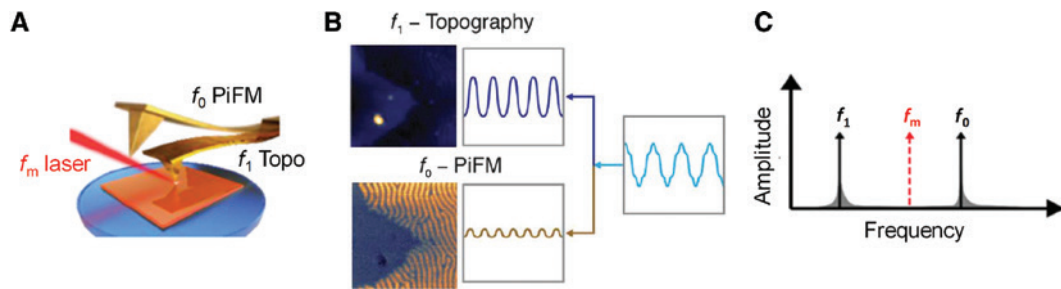
Figure 4: Enhancement of signal by using multiple mechanical resonances of the cantilever [26, 47].
(A) Schematic diagram of sideband driven enhancement for photo-induced force microscopy (PiFM). (B) Cantilever's position decomposed into eigenmodes with the frequency of f_1 (up) and f_0 (down), which provides the information of topography and photo-induced force respectively. (C) Photo-induced force (right peak) and its sideband (left peak) modulated by the cantilever's oscillation (dashed arrow in red) in frequency domain (Figures adapted from Refs. [26, 47]).

In contrast, low signal-to-noise ratios are observed when the laser repetition rate is off-resonance from the mechanical resonances of the cantilever (Figure 3C).

Sometimes, the repetition rate of the illumination pulsed laser is tuned not to match any of the mechanical resonances, but the difference of two mechanical resonances. In Ref. [26], the cantilever measures mainly the photo-induced gradient force, where the AFM cantilever is initially driven at its fundamental mechanical resonance f_0, and the incoming laser's repetition rate is chosen at f_1–f_0 (Figure 4). The photo-induced force, influenced by the tip-sample distance, is modulated by the cantilever's oscillation at the frequency of f_0, and therefore creating a sideband at f_1 (Figure 4C). The oscillation of the AFM cantilever at f_1
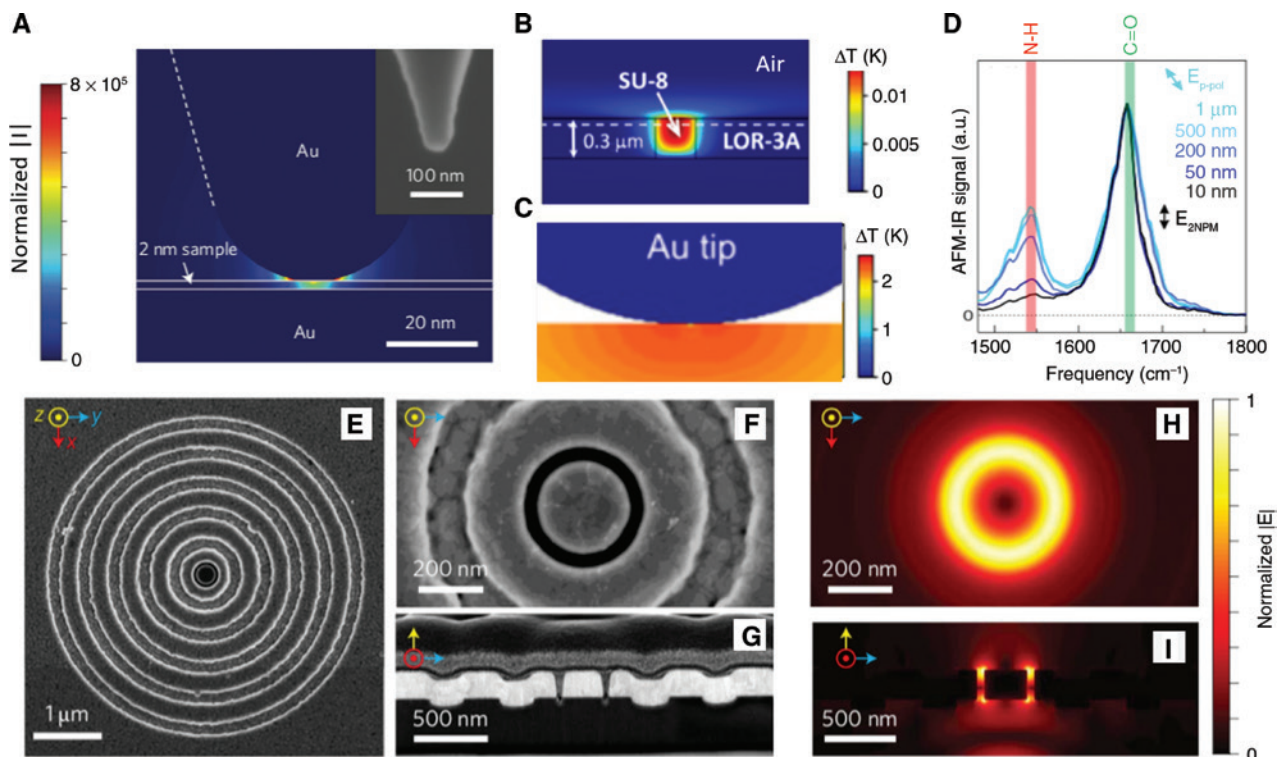
Figure 5: Plasmonic nanostructures to enhance microscopic optical forces [55, 57, 59, 60].
(A) Optical field simulation of monolayer sample with the thickness of 2 nm. (B) Simulation of temperature elevation of sample with the thickness of 0.3 μm enhanced by a gold tip. (C) Temperature simulation of sample with the thickness of 10 nm. (D) AFM-IR spectra acquired on purple-membrane films of various thickness from 10 nm to 1 μm. (E–G) Scanning electron microscopy (SEM) images of bull's eye grating-flanked coaxial nanoaperture. (H, I) Finite difference time domain simulations of the field distribution on resonance of the nanoaperture (Figures adapted from Refs. [55, 57, 59, 60]).

is a result of the measured optical force, enhanced by the second mechanical resonance of the cantilever (Figure 4B).

3.1.4 Enhancing the signal-to-noise ratio using plasmonic resonance

To enhance the signal-to-noise ratio, especially in detecting monolayers of molecules, plasmonic resonances in particular gap plasmons were employed. Reference [55] shows that the 2 nm gap between a sharp gold-coated AFM tip and a gold coated substrate is able to boost optical field intensity by as high as 2×10^5 times.

Strongly localized field from plasmonic resonances can also create a hotspot in the monolayer of samples. Due to this effect, the temperature increase of a 10-nm film is shown to be ~200 times larger than a 300-nm film [55, 59, 60]. The decreased thermal expansion due to the reduced thickness is complemented by the temperature increase due to the optical field enhancement. Therefore,

the signal-to-noise ratio of the spectra acquired on purple-membrane films of different thickness is similar as shown in Figure 5D. In a separate study, Figure 5E–I, a concentric bull's-eye grating is adapted to boost the transmission through a coaxial plasmonic aperture [57].

4 Applications

With the high spatial resolution (~10 nm) and force sensitivity (piconewton regime), optical-induced force microscopy is used to identify chemical bonds, monolayers of molecules, and even structural information.

4.1 Detecting chemical components

The mid-IR absorption spectrum in the 400–4000 cm^{-1} region serves as the chemical fingerprints that provide
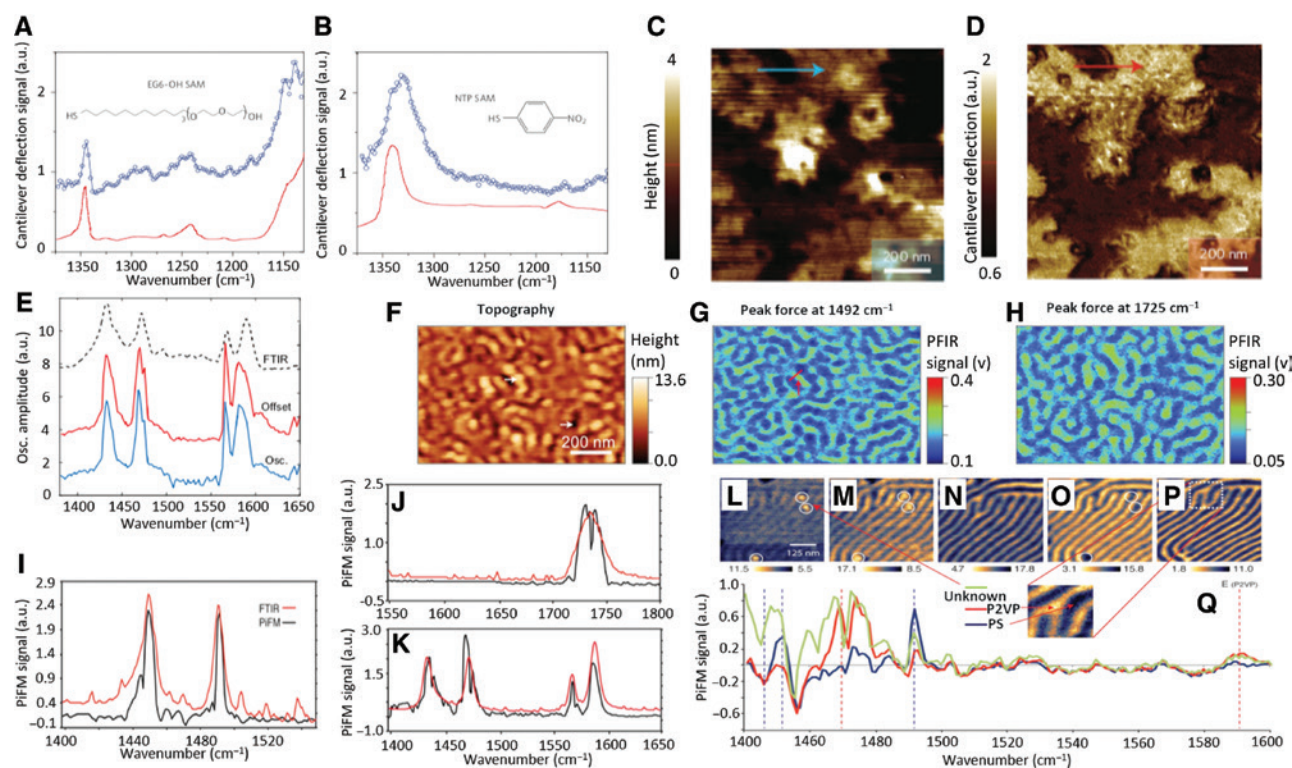
Figure 6: Chemical detection of molecular thin films [26, 55, 56].
(A, B) AFM-IR spectra (blue curve) and FTIR spectra (red curve) of self-assembled monolayer of two types of molecules ethylene glycol (EG6-OH) and 4-nitrothiophenol molecules. (C) AFM topography of monolayer of PEG molecules. (D) AFM-IR imaging of PEG molecules at 1342 cm^{-1}. (E) Peak-force IR(PFIR) spectra based on the oscillation amplitude of contact resonance (blue curve) and baseline offset (red curve) with FTIR spectra (dashed curve) as a reference. (F) Topography of poly(styrene-b-methyl methacrylate (PS-b-PMMA) block copolymer. (G) PFIR image at the IR frequency of 1725 cm^{-1}. (H) PFIR image at the IR frequency of 1725 cm^{-1}. (I–K) PiFM spectra (black curve) and FTIR spectra (red curve) of homopolymers polystyrene (PS), PMMA, and P2VP. (L–P) PiFM images of PS-b-poly(2-vinyl pyridine) (P2VP) at 1447, 1452, 1469, 1492, and 1589 cm^{-1}. (Q) The PiFM spectra of P2VP, PS, and an unknown material taken from the area circled in P (Figures adapted from Refs. [26, 55, 56]).

important information for chemical composition, chemical bond, and structures. Fourier transform spectroscopy (FTIR) is an important tool for spectral measurement. A widely used FTIR database is well established for chemical identification in chemistry, biology, and medicine [61]. In conventional FTIR, the spatial resolution for FTIR is limited by the diffraction limit, which is the micrometer regime. With the help of IR scattering NSOM technique, a high spatial resolution FTIR, nano-FTIR, is developed [62, 63]. However, the signal-to-noise ratio of nano-FTIR is limited by the incident light scattering. As a result, lock-in signal demodulation is often needed, and only limited types of samples, mainly on polymers with strong IR resonances, are measured.

On the other hand, AFM-IR combines AFM with IR spectroscopy, showing a spatial resolution ~100 nm. Figure 6A–D shows the detection of the chemical bonds from monolayers of molecules using a technique similar to AFM-IR. The measurement is done by an AFM tip in contact with the sample and excited by a QCL instead of a free electron laser; the local electromagnetic field is enhanced by plasmonic gap modes [55]. For hydroxyl-terminated hexa (ethylene glycol) undecanethiol molecules, the absorption bands corresponding to CH_2 wagging (at 1352 cm^{-1}) and twisting (1244 cm^{-1}) modes was observed

(Figure 6A). For 4-nitrothiophenol molecules, a strong peak around 1339 cm^{-1} corresponding to NO_2 stretching mode was observed (Figure 6B). High resolution microscopy of polyethylene glycol monolayer islands was mapped by scanning with laser wavenumber of 1342 cm^{-1} as shown in Figure 6D, which matches with the topography in Figure 6C.

Figure 6E–H shows PFIR and FTIR spectrum of poly(2-vinyl pyridine) (P2VP), topography and PFIR microscopy of poly(styrene-b-methyl methacrylate) (PS-b-PMMA) block copolymer). The measurement is made by an AFM tip in tapping mode and the IR laser source is a QCL [56]. As shown in Figure 6E, for P2VP, the thermal induced offset and oscillating amplitude of the AFM tip both show good correlation to the FTIR spectrum. Figure 6F–H shows the topography of the copolymer using PFIR at 1492, and 1725 cm^{-1} (1492 cm^{-1} is on resonance with the polystyrene (PS) domains, and 1725 cm^{-1} is a characteristic feature of C=O group in PMMA).

Figure 6I–K shows the spectrum of homopolymers PS, PMMA, and P2VP, measured with PiFM; these spectra match well with the FTIR spectrum [26]. The measurement is made by AFM in tapping mode, a QCL illuminates the sample with a repetition rate matching the frequency difference between the first and second mechanical
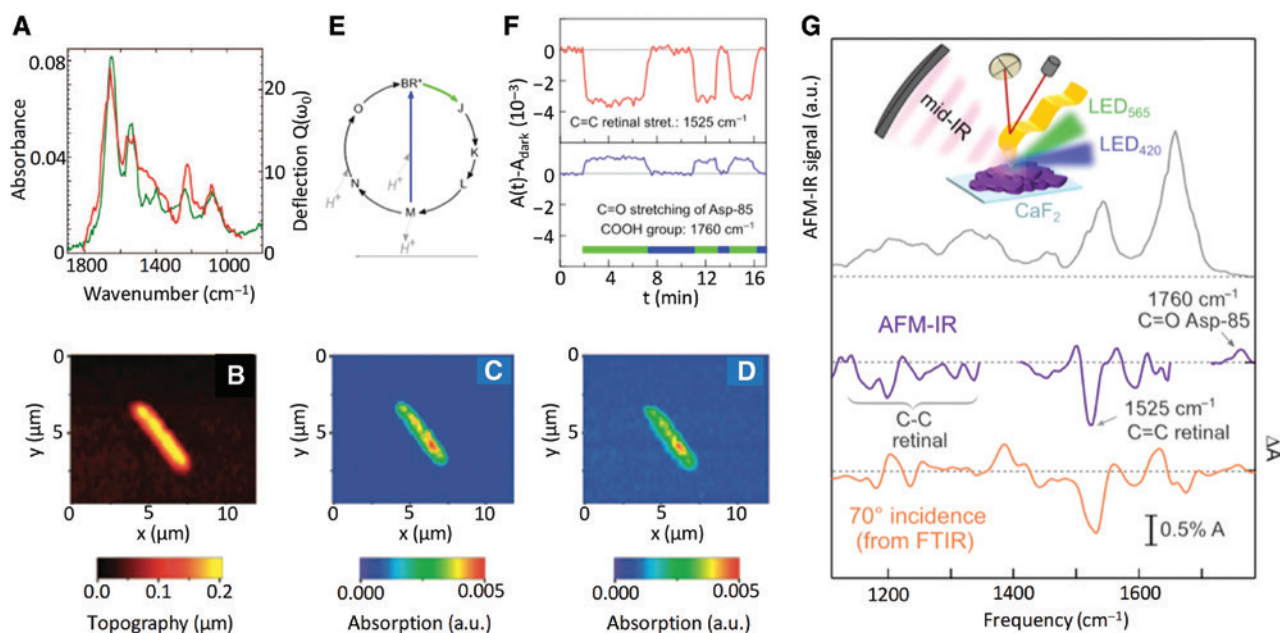
Figure 7: Microscopy for biological samples [23, 60].
(A) FTIR spectra of an *Escherichia coli* culture and (green curve) AFM-IR spectrum of a single *E. coli* bacterium. (B–D) Topography, AFM-IR image at 1660 cm^{-1} (amide I absorption peak), and AFM-IR image at 1240 cm^{-1} (amide III absorption peak). (E) Bacteriorhodopsin photocycle. (F) FTIR signal at 1525 (C=C peak) and 1760 cm^{-1} (COOH group peak) while alternately turning on and off the green and blue LEDs after a 2 min dark period. (G) AFM-IR spectrum of a thick-film region ($d = 1 \mu m$) located in a purple-membrane (gray curve), AFM-IR difference-spectra $\Delta A = A_{green} - A_{blue}$ (violet curve), and FTIR difference-spectrum; the schematic of experiment is shown above.

resonances of the cantilever. The microscopy image of PS-b-P2VP is obtained at wavenumber of 1447, 1452, 1469, 1492, and 1589 cm⁻¹ (Figure 6L–P). The absorption bands of P2VP, PS, and an unknown third component are shown in Figure 6Q.

4.2 Measuring biological processes

Using AFM-IR, the spectrum of a single *Escherichia coli* bacterium matches well with the FTIR spectrum of an *E. coli* culture (Figure 7A) [23]. The high spatial resolution of AFM-IR enables chemical imaging of single cells as shown

in Figure 7C–D. AFM-IR is also used to study the proton pump activity of bacteriorhodopsin (BR) in Ref. [60]. As shown in Figure 7E, in a BR photocycle, green light initiates the transition from the dark states (BR*) to intermediate states (J, K, L), until proton release toward the extracellular side (M); and blue light brings proteins back to the dark states (BR*). As shown in Figure 7F, the specific FTIR spectra of a thick film of native purple membranes reveal such chemical transitions. The AFM-IR difference-spectra of a thick-film region shows good matching with the FTIR difference-spectra, which gives important evidence of the reaction under the illumination of green and blue light.
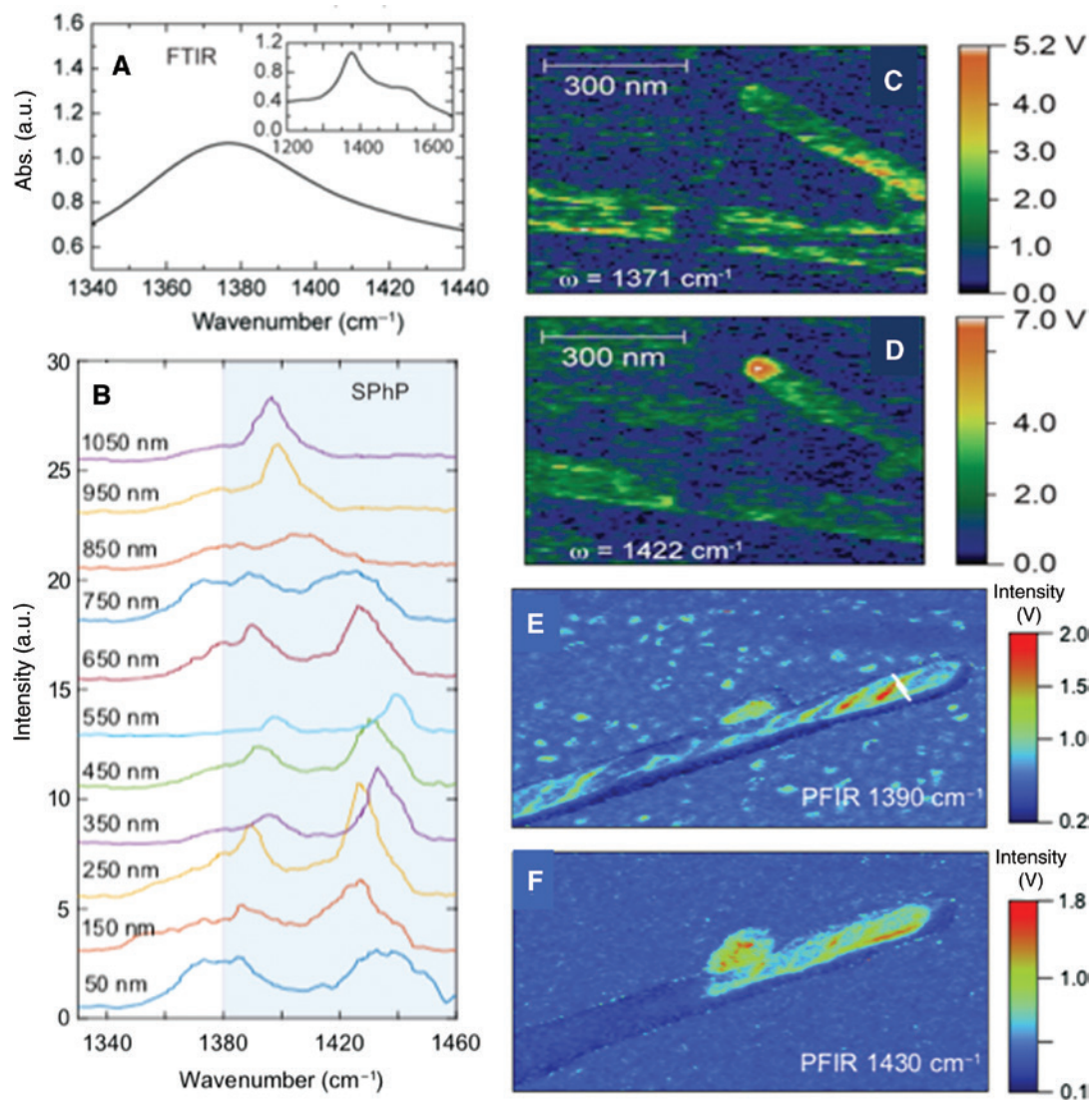
Figure 8: Spectrum and microscopy images of boron nitride nanotubes (BNNTs) [56, 64].
(A) FTIR spectrum of BNNTs; the inset shows a FTIR spectrum of a bigger range. (B) PFIR at different locations away from the BNNT terminal, showing the position-dependent surface phonon polariton resonances. (C–D) Nano-FTIR images of BNNTs at 1371 and 1422 cm⁻¹. (E, F) PFIR images of BNNTs at 1390 and 1430 cm⁻¹. The spatial resolution of both nano-FTIR and PFIR is ~10 nm.

4.3 Identifying inorganic nanoparticles

Nano-FTIR, which is used to detect the spectrum of boron nitride nanotubes (BNNTs) (Figure 8A [64]), shows the phonon resonances but not the surface phonon polariton resonances which is detected by PFIR (Figure 8B [56]). The PFIR micrograph of BNNTs shows stronger absorption near its terminal with wavenumber around 1430 cm⁻¹, which is detected by both nano-FTIR in Figure 8C–D [64] and PFIR in Figure 8E–F [56]. The strong absorption at
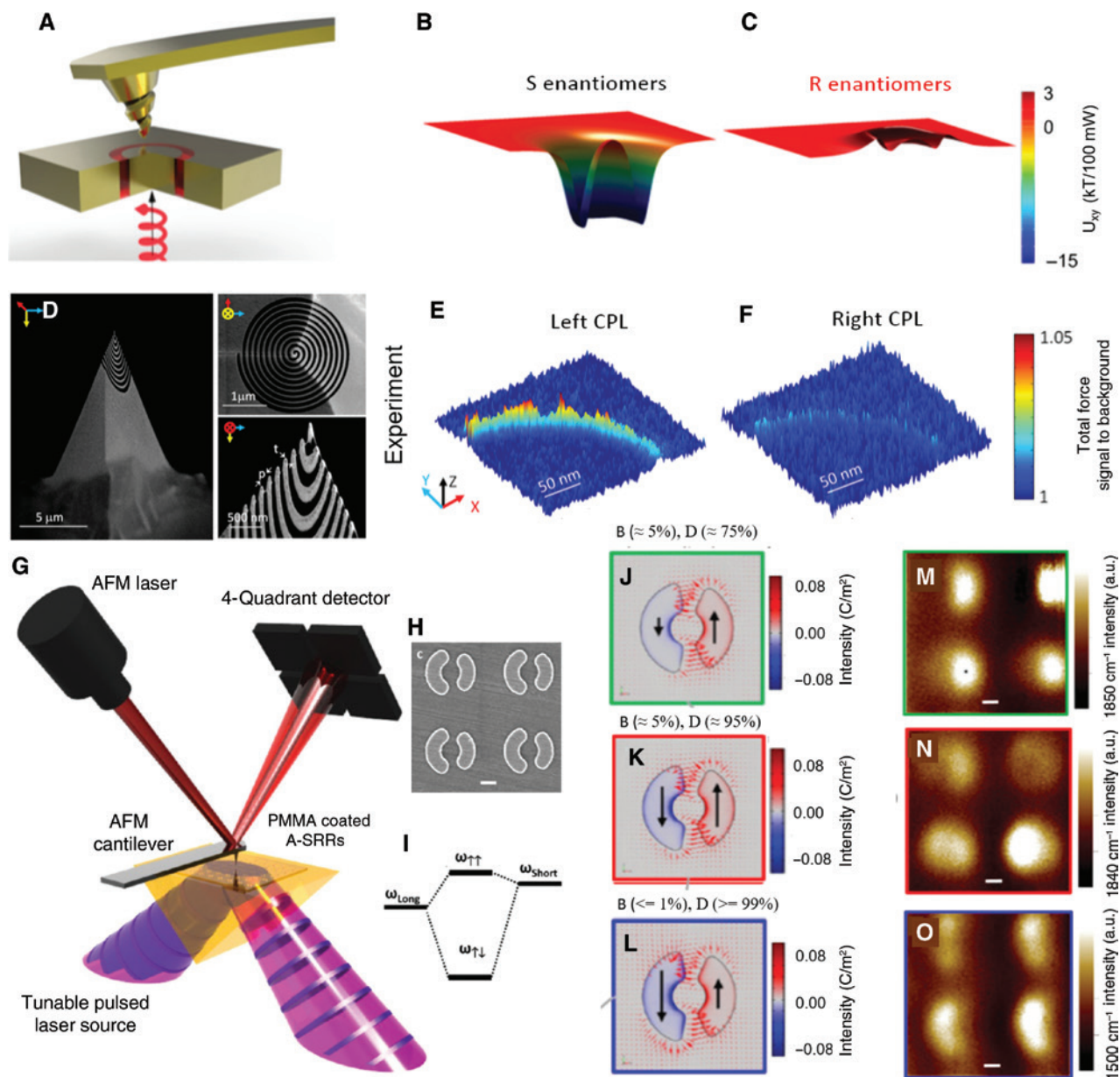
Figure 9: Enantioselective optical force microscopy [57, 65, 66].
(A) Schematic illustration of circularly polarized light (CPL) illuminate on coaxial plasmonic nano-aperture. (B, C) Simulated 2D trapping potential for enantiomers using the coaxial plasmonic aperture. The chirality of the enantiomer is assumed to be $\kappa = \pm 0.6$, and the incidence is left-CPL. (D) SEM image of the chiral AFM tip (with left handedness). (E, F) Optical force map on the coaxial nano-aperture with left- and right-handed CPL incidence. (G) Schematic illustration of the PTIR measurement. Asymmetric split ring resonators (A-SSRs) are coated with PMMA. When IR laser pulses are absorbed by the sample (PMMA coated A-SRRs), the sample rapidly expands and deflects the AFM cantilever; the amplitude of the deflection is proportional to the absorbed energy. (H) SEM of the A-SRRs. (I) Frequency splitting due to coupling between the long and short SRRs. (J–L) Electric field distribution of different mixture of bright-mode and dark-mode with various ratio. (M–O) PTIR at the wavenumber of 1850 (mixture of dark- and bright-mode), 1500 (dark-mode), and 1191 cm⁻¹ (mixture of dark- and bright-mode. PMMA CH₃ wagging mode) (Figures adapted from Refs. [57, 65, 66]).

the terminal likely indicates a different BNNT structure. The structure might be less constrained at the end of the nanotube. For example, a larger separation between constituent BN layers than the tube shaft corresponds to a weakened LO-TO splitting. As a result, the transverse optical mode shifts to higher frequency.

4.4 Imaging plasmonic hot spots and chiral structures

Plasmonic nanostructures can give rise to locally enhanced fields and field gradient, therefore, enhancing the signal-to-noise ratio of optical-force microscopy. As shown in Figure 9B–C, a coaxial plasmonic nano-aperture generates strong field gradient close to the transmission side of the aperture [65]. When illuminated with circularly polarized light (CPL), selective trapping potentials can be exerted on enantiomers (chiral structures with opposite handedness). When illuminated with left CPL, left-hand enantiomer experiences a trapping potential, while the opposite enantiomer is repelled by a potential barrier. Reference [57] demonstrated this result experimentally. A coaxial plasmonic aperture is illuminated from the bottom with CPL, while a nanostructured chiral AFM tip scans across the nanoaperture on the transmission side (scanning electron microscopic image of a left-hand chiral AFM tip is shown in Figure 9D). The chiral AFM tip can experience a differential optical force when comparing its measured forces exerted with left-CPL and right-CPL illumination (Figure 9E–F).

In Ref. [66], PTIR is employed to image the surface plasmon modes of the asymmetric structures. As shown in Figure 9G, PMMA is coated on the surface of the asymmetric split-ring resonators. As the absorption is proportional to the optical field intensity, the PTIR images in Figure 9M–O shows good correspondence with the optical field distribution shown in Figure 9J–L.

5 Conclusions and perspectives

Here we summarized the fundamental theories of light-induced forces, in particular, gradient forces, scattering forces, and photo-thermal forces. When combined with AFM, these forces can detect material properties with a spectral resolution up to 8 cm^{-1} [23] and a spatial resolution approaching 10 nm [55, 56]. We discussed a few recently developed light-induced microscopy techniques, including PiFM, AFM-IR, PTIR, PFIR, and COFM, each of which has advantages towards a unique application.

When ultrafast light source is used, single point measurement can be potentially achieved in femtosecond time frame [67], however, temporal resolution of the imaging is still limited by either laser repetition rate and/or tip-scanning rate and, therefore, most demonstrated images are in the temporal scales of seconds. Future directions toward improving temporal resolutions can be of great importance to study dynamic processes.

References

[1] Binnig G, Rohrer H, Gerber C, Weibel E. Surface studies by scanning tunneling microscopy. Phys Rev Lett 1982;49:57–61.

[2] Binnig G, Quate CF, Gerber C. Atomic force microscope. Phys Rev Lett 1986;56:930–3.

[3] Knoll B, Keilmann F. Near-field probing of vibrational absorption for chemical microscopy. Nature 1999;399:134–7.

[4] Hillenbrand R, Keilmann F. Complex optical constants on a subwavelength scale. Phys Rev Lett 2000;85:3029–32.

[5] Dai GB, Yang ZB, Geng GS, et al. Signal detection techniques for scattering-type scanning near-field optical microscopy. Appl Spectrosc Rev 2018;53:806–35.

[6] Bazylewski P, Ezugwu S, Fanchini G. A review of three-dimensional scanning near-field optical microscopy (3D-SNOM) and its applications in nanoscale light management. Appl Sci-Basel 2017;7:973.

[7] Hecht B, Sick B, Wild UP, et al. Scanning near-field optical microscopy with aperture probes: fundamentals and applications. J Chem Phys 2000;112:7761–74.

[8] Murdick RA, Morrison W, Nowak D, Albrecht TR, Jahng J, Park S. Photoinduced force microscopy: a technique for hyperspectral nanochemical mapping. Jpn Appl Phys 2017;56:08LA04.

[9] Zenhausern F, Martin Y, Wickramasinghe HK. Scanning interferometric apertureless microscopy: optical imaging at 10 angstrom resolution. Science 1995;269:1083.

[10] Pohl DW, Denk W, Lanz M. Optical stethoscopy: image recording with resolution λ/20. Appl Phy Lett 1984;44:651–3.

[11] Ashkin A. Acceleration and trapping of particles by radiation pressure. Phys Rev Lett 1970;24:156–9.

[12] Ashkin A, Dziedzic JM, Bjorkholm JE, Chu S. Observation of a single-beam gradient force optical trap for dielectric particles. Opt Lett 1986;11:288–90.

[13] Ashkin A, Dziedzic JM. Optical levitation by radiation pressure. Appl Phys Lett 1971;19:283–5.

[14] Ashkin A. History of optical trapping and manipulation of small-neutral particle, atoms, and molecules. IEEE Selected Topics Quant Electron 2000;6:841–56.

[15] Neuman KC, Block SM. Optical trapping. Rev Sci Instrum 2004;75:2787–809.

[16] Ashkin A, Dziedzic J. Optical trapping and manipulation of viruses and bacteria. Science 1987;235:1517–20.

[17] Righini M, Zelenina AS, Girard C, Quidant R. Parallel and selective trapping in a patterned plasmonic landscape. Nat Phys 2007;3:477–80.

[18] Novotny L, Bian RX, Xie XS. Theory of nanometric optical tweezers. Phys Rev Lett 1997;79:645–8.

[19] Okamoto K, Kawata S. Radiation force exerted on sub-wavelength particles near a nanoaperture. Phys Rev Lett 1999;83:4534–7.

[20] Chen J, Ng J, Lin Z, Chan CT. Optical pulling force. Nat Photon 2011;5:531.

[21] Chaumet PC, Rahmani A, Nieto-Vesperinas M. Optical trapping and manipulation of nano-objects with an apertureless probe. Phys Rev Lett 2002;88:123601.

[22] Dazzi A, Glotin F, Carminati R. Theory of infrared nanospectroscopy by photothermal induced resonance. J Appl Phys 2010;107:124519.

[23] Dazzi A, Prater CB, Hu Q, Chase DB, Rabolt JF, Marcott C. AFM–IR: combining atomic force microscopy and infrared spectroscopy for nanoscale chemical characterization. Appl Spectrosc 2012;66:1365–84.

[24] Jahng J, Kwon H, Lee ES. Photo-induced force microscopy by using quartz tuning-fork sensor. Sensors 2019;19:1530.

[25] Jahng J, Potma EO. Dynamic photo-induced force microscopy. MRS Proc 2015;1754:103–8.

[26] Nowak D, Morrison W, Wickramasinghe HK, et al. Nanoscale chemical imaging by photoinduced force microscopy. Sci Adv 2016;2:e1501571.

[27] Stratton JA. Electromagnetic theory, First ed. New York: MacGraw-Hill Book Company, 1941.

[28] Jackson JD. Classical electrodynamics, Third ed. Berkeley, CA: John Wiley & Sons, 2001.

[29] Richards D, Zayats A, Nieto-Vesperinas M, Chaumet PC, Rahmani A. Near-field photonic forces. Philos R Lond Ser A Math Eng Sci 2004;362:719–37.

[30] Gordon JP. Radiation forces and momenta in dielectric media. Phys Rev A 1973;8:14–21.

[31] Chaumet PC, Nieto-Vesperinas M. Time-averaged total force on a dipolar sphere in an electromagnetic field. Opt Lett 2000;25:1065–7.

[32] Arias-Gonzalez JR, Nieto-Vesperinas M. Optical forces on small particles: attractive and repulsive nature and plasmon-resonance conditions. J Opt Soc Am A Opt Image Sci Vis 2003;20:1201–9.

[33] Bekshaev AY. Subwavelength particles in an inhomogeneous light field: optical forces associated with the spin and orbital energy flows. J Opt 2013;15:044004.

[34] Bekshaev AY. Corrigendum: subwavelength particles in an inhomogeneous light field: optical forces associated with the spin and orbital energy flows. J Opt 2016;18:029501.

[35] Nieto-Vesperinas M, Sáenz JJ, Gómez-Medina R, Chantada L. Optical forces on small magnetodielectric particles. Opt Exp 2010;18:11428–43.

[36] Canaguier-Durand A, Hutchison JA, Genet C, Ebbesen TW. Mechanical separation of chiral dipoles by chiral light. New J Phys 2013;15:123037.

[37] Canaguier-Durand A, Genet C. Chiral route to pulling optical forces and left-handed optical torques. Phys Rev A 2015;92:043823.

[38] Liberal I, Ederra I, Gonzalo R, Ziolkowski RW. Electromagnetic force density in electrically and magnetically polarizable media. Phys Rev A 2013;88:053808.

[39] Cameron RP, Barnett SM, Yao AM. Discriminatory optical force for chiral molecules. New Phys 2014;16:013020.

[40] Wang SB, Chan CT. Lateral optical force on chiral particles near a surface. Nat Commun 2014;5:3307.

[41] Kamandi M, Albooyeh M, Veysi M, et al. Unscrambling structured chirality with structured light at the nanoscale using photoinduced force. ACS Photon 2018;5:4360–70.

[42] Patti F, Saija R, Denti P, et al. Chiral optical tweezers for optically active particles in the T-matrix formalism. Sci Rep 2019;9:29.

[43] Hayat A, Mueller JPB, Capasso F. Lateral chirality-sorting optical forces. Proc Natl Sci 2015;112:13190.

[44] Alizadeh MH, Reinhard BM. Transverse chiral optical forces by chiral surface plasmon polaritons. ACS Photons 2015;212:1780–8.

[45] Zeng J, Huang F, Guclu C, et al. Sharply focused azimuthally polarized beams with magnetic dominance: near-field characterization at nanoscale by photoinduced force microscopy. ACS Photon 2018;5:390–7.

[46] Rukhlenko ID, Tepliakov NV, Baimuratov AS, et al. Completely chiral optical force for enantioseparation. Sci Rep 2016;6:36884.

[47] Jahng J, Potma EO, Lee ES. Tip-enhanced thermal expansion force for nanoscale chemical imaging and spectroscopy in photoinduced force microscopy. Anal Chem 2018;90:11054–61.

[48] Yang HU, Raschke MB. Resonant optical gradient force interaction for nano-imaging and -spectroscopy. New J Phys 2016;18:053042.

[49] Jahng J, Brocious J, Fishman DA, et al. Gradient and scattering forces in photoinduced force microscopy. Phys Rev B 2014;90:155417.

[50] Rajapaksa I, Uenal K, Wickramasinghe HK. Image force microscopy of molecular resonance: amicroscope principle. Appl Phys Lett 2010;97:073121.

[51] Huang F, Ananth Tamma V, Mardy Z, Burdett J, Kumar Wickramasinghe H. Imaging nanoscale electromagnetic near-field distributions using optical forces. Sci Rep 2015;5:10610.

[52] Rajapaksa I, Kumar Wickramasinghe H. Raman spectroscopy and microscopy based on mechanical force detection. Appl Phys Lett 2011;99:161103–33.

[53] Tam AC. Applications of photoacoustic sensing techniques. Mod Phys 1986;58:381.

[54] Lahiri B, Holland G, Centrone A. Chemical imaging beyond the diffraction limit: experimental validation of the PTIR technique. Small 2013;9:439–45.

[55] Lu F, Jin M, Belkin MA. Tip-enhanced infrared nanospectroscopy via molecular expansion force detection. Nat Photon 2014;8:307–12.

[56] Wang L, Wang H, Wagner M, Yan Y, Jakob DS, Xu XG. Nanoscale simultaneous chemical and mechanical imaging via peak force infrared microscopy. Sci Adv 2017;3:e1700255.

[57] Zhao Y, Saleh AAE, van de Haar MA, et al. Nanoscopic control and quantification of enantioselective optical forces. Nat Nanotechnol 2017;12:1055–9.

[58] Wang L, Wang H, Vezenov D, Xu XG. Direct measurement of photoinduced force for nanoscale infrared apectroscopy and chemical-sensitive imaging. Phys Chem C 2018;122:23808–13.

[59] Lu F, Belkin MA. Infrared absorption nano-spectroscopy using sample photoexpansion induced by tunable quantum cascade lasers. Opt Exp 2011;19:19942–7.

[60] Giliberti V, Polito R, Ritter E, et al. Tip-infrared difference-nanospectroscopy of the pump activity of bacteriorhodopsin in purple membrane patches. Nano Lett 2019;19:3014–114.

[61]   Griffiths PR, Haseth JAD. Fourier transform infrared spectro-
       metry, 2nd ed. England: Wiley-Interscience, 2006.
[62]   Huth F, Govyadinov A, Amarie S, Nuansing W, Keilmann
       F, Hillenbrand R. Nano-FTIR absorption spectroscopy of
       molecular fingerprints at 20 nm spatial resolution. Nano Lett
       2012;12:3973–8.
[63]   Huth F, Schnell M, Wittborn J, Ocelic N, Hillenbrand R. Infrared-
       spectroscopic nanoimaging with a thermal source. Nat Mater
       2011;10:352–6.
[64]   Xu XG, Tanur AE, Walker GC. Phase controlled homodyne infra-
       red near-field microscopy and spectroscopy reveal inhomoge-

neity within and among individual boron nitride nanotubes. J
Phys Chem A 2013;117:3348–54.
[65]   Zhao Y, Saleh AA, Dionne JA. Enantioselective optical trapping
       of chiral nanoparticles with plasmonic tweezers. ACS Photon
       2016;3:304–9.
[66]   Lahiri B, Holland G, Aksyuk V, Centrone A. Nanoscale imaging
       of plasmonic hot spots and dark modes with the photothermal-
       induced resonance technique. Nano Lett 2013;13:3218–24.
[67]   Berweger S, Atkin JM, Olmon RL, Raschke MB. Light on the tip
       of a needle: plasmonic nanofocusing for spectroscopy on the
       nanoscale. Phys Chem Lett 2012;3:945–52.